SCIENTIFIC REPORTS
nature research

OPEN

Fast response of complementary electrochromic device based on WO_3/NiO electrodes

Po-Wen Chen[1] ✉, Chen-Te Chang[1], Tien-Fu Ko[1], Sheng-Chuan Hsu[1], Ke-Ding Li[2] & Jin-Yu Wu[1]

Nanoporous structures have proven as an effective way for enhanced electrochromic performance by providing a large surface area can get fast ion/electron transfer path, leading to larger optical modulation and fast response time. Herein, for the first time, application of vacuum cathodic arc plasma (CAP) deposition technology to the synthesis of WO_3/NiO electrode films on ITO glass for use in fabricating complementary electrochromic devices (ECDs) with a ITO/WO_3/$LiClO_4$-Perchlorate solution/NiO/ITO structure. Our objective was to optimize electrochromic performance through the creation of electrodes with a nanoporous structure. We also examined the influence of WO_3 film thickness on the electrochemical and optical characteristics in terms of surface charge capacity and diffusion coefficients. The resulting 200-nm-thick WO_3 films achieved ion diffusion coefficients of (7.35×10^{-10} (oxidation) and 4.92×10^{-10} cm^2/s (reduction)). The complementary charge capacity ratio of WO_3 (200 nm thickness)/NiO (60 nm thickness) has impressive reversibility of 98%. A demonstration ECD device (3×4 cm^2) achieved optical modulation (ΔT) of 46% and switching times of 3.1 sec (coloration) and 4.6 sec (bleaching) at a wavelength of 633 nm. In terms of durability, the proposed ECD achieved ΔT of 43% after 2500 cycles; i.e., 93% of the initial device.

Over the past decades, electrochromic devices (ECDs) have been used in energy efficient buildings, optical information displays, variable-reflectance mirrors, switchable mirrors, and electronic papers[1–5]. Electrochromism materials change their optical characteristics (transmittance, reflectance, and absorption) reversibly through applying a dc voltage[6]. Electrochromism has attracted much attention because it could provide a tremendous promising application in energy-saving smart windows. Smart windows based on electrochromic (EC) materials easily control the indoor sunlight and solar heat and can be effectively reduced the heating or cooling loads of building interiors[6]. A wide variety of electrochromic materials have been developed, including metal oxides[7–9], small organic molecules[10], and conductive polymer thin films[11–13]. Complementary ECDs are composed of anodic and cathodic coloring materials in a five-layer structure. A pair of transparent conducting layers sandwich an ionic conduction layer (electrolyte) in contact with an electrochromic (EC) layer and an ion storage (complementary) layer[14–16]. Tungsten oxide (WO_3) is known as one of the most popular cathodic coloration material and nickel oxide (NiO) as typical anodic coloration material, which has been intensively investigated[14–17].

WO_3 film is a transition metal oxide, which can be reversibly switched between colorless and blue under positive or negative voltage, respectively[18,19]. The chemical reaction underlying the electrochromic behavior of WO_3 films is based on reversible oxidation/reduction reactions induced by the electrochemical double injection/extraction of positive ions (lithium or proton) and electrons into/out of the host WO_3 lattice in the transition from W^{5+} to W^{5+} [19,20]. WO_3 films have been fabricated in a variety of nanostructures, including nano-rods[19,21,22], nanosheets[20], and nanotrees[23]. Note however that a dense structure, low diffusion coefficient, and/or long diffusion length for ion insertion tend to hinder optical modulation performance. By increasing the contact area between the electrode and electrolyte, nanoporous WO_3 structures reduce the diffusion path of ions and providing channels to facilitate the rapid transfer of ion/electrons, resulting in particularly good electrochromic and electrochemical performance[19,20,23]. Electrochromic WO_3 films have been fabricated using a variety of methods, including sputtering[24–27], chemical vapor deposition (CVD)[28–30], spray pyrolysis[31,32], thermal evaporation[33], electron-beam deposition[34], and sol-gel[35–37] methods. Lee *et al.*[19] recently reported on the synthesis of uniform WO_3 nano-rods, resulting in films with fast coloration/bleaching times (28.8/4.5 sec at 633 nm). Zhang *et al.*[23]

[1]Division of Physics, Institute of Nuclear Energy Research, Taoyuan County, 32546, Taiwan. [2]Department of Materials Science and Engineering, National Cheng Kung University, Tainan, 70101, Taiwan. ✉e-mail: powen@iner.gov.tw

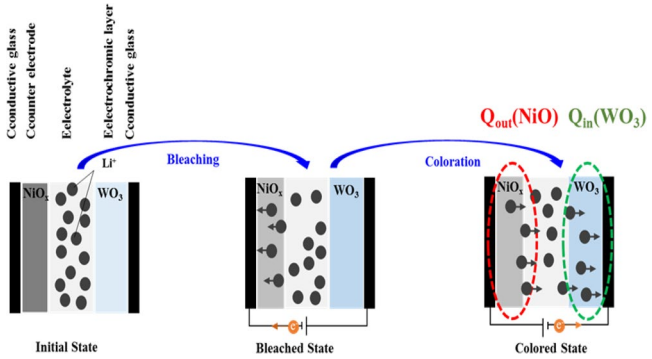

Figure 1. Working principles for ECD. Schematic diagram of coloration and bleaching process of with WO_3 electrochromic layer and NiO counter layer.

used thermal annealing in the synthesis of WO_3 electrodes within a one-dimensional structure, which resulted in good CE (43.6 cm^2/C), and fast coloration/bleaching times (7.6/4.2 sec at 633 nm).

Different above technology, in the current study, we used cathodic arc plasma (CAP) technology to fabricate WO_3/NiO films with a porous surface structure with the aim of enhancing electrochromic performance and accelerating switching speeds[38–41]. We also examined the degree to which the thickness of WO_3 layers affects the electrochemical and optical properties of ECDs.

Results

Electrochromic mechanism for NiO-WO_3 system. As shown in Fig. 1(a–c), the application of voltage (an electric field) to the device causes positive ions to move toward the electric field, while the electrons move in the opposite direction. The movement of ions (electrons) into the electrochromic (ion storage) layers is responsible for the coloration (bleaching) of the ECDs. The underlying physics involved in the electrochromic reactions can be represented using the following the redox equations:

$$WO_3(\text{bleaching}) + x(M^+ + e^-) \leftrightarrows M_xWO_3(\text{coloration}), \quad (1)$$

where M indicates the lithium ions (Li^+) or hydrogen ions (H^+) ions. The WO_3 thin film changes from transparent to deep blue under the effects of electron insertion (i.e., photo-effected intervalence electron transfer from W^{6+} to W^{5+} sites). The electrochromic mechanism governing the behavior of Li^+ ions against ion insertion/extraction in the NiO electrode can be represented using the following the redox equations:

$$NiO_x + y(M^+ + e^-) \rightarrow M_yNiO_x,\ M_yNiO_x(\text{coloration})M_{y-z}NiO_x(\text{bleaching}) + z(M^+ + e^-). \quad (2)$$

The reduction of Ni^{3+} to Ni^{2+} leads to the bleaching of the NiO film (during the cathodic scan), and coloration of NiO film via the oxidation of Ni^{2+} to Ni^{3+} (in the reverse process). Continuously applying negative voltage to the NiO electrode (ion storage layer) causes the insertion of electrons and Li^+ ions leading to the oxidation of Ni^{2+} to Ni^{3+}, with the result that the coloration state is dominant. In Fig. 1(c), for test step, to understand surface charge capacity for WO_3/NiO electrode films, which were integrated CA curves defined as both intercalation surface charges (Q_{in}) and extraction surface charges (Q_{out}). Here, the complementary surface charge capacity ratio R is defined as the insertion WO_3 electrode divided by the extraction NiO electrode.

WO_3/ITO and NiO/ITO films: surface charge capacity ratio. The complementary ECD in the current study included two electrochromic electrodes, as in thin-film batteries. Thus, we calculated the surface charge capacity ratio of the electrodes in both directions. We first sought to elucidate the electrochemical and energy storage properties of the WO_3/ITO/glass by constructing three electrode cells, which comprised a working electrode (WO_3 film on ITO/glass), a counter-electrode (Pt mesh) and a reference electrode (Ag/AgCl) in 0.5 M $LiClO_4$/Perchlorate ($LiClO_4$/PC) solution.

The surface charge capacity of the WO_3 layers was based on integral to CA curves was carried with from −1.5 to 0.3 V versus AgCl/Ag in intercalation surface charges (Q_{in}) and extraction surface charges (Q_{out}). As shown in Fig. 2(a), the 200-nm-thick WO_3 electrode returned the following values: Q_{in} (7.38 mC cm^{-2}), Q_{out} (8.4 mC cm^{-2}), and reversibility, Q_{in}/Q_{out} is about 87% better than the other samples. Here, complementary charge capacity ratio R is defined as the intercalation WO_3 electrode divided by the extraction NiO electrode according to following equation:

$$R = Q_{in}(WO_3)/Q_{out}(NiO), \quad (3)$$

where Q_{in} (WO_3) is the surface charge capacity of the WO_3 electrode during intercalation and Q_{out} (NiO) is the surface charge capacity of the NiO electrode during the extraction process. Q_{out} (NiO) was carried with from 0.7 V versus Ag/AgCl and observed Q_{out} (NiO) value is 7.45 mC cm^{-2}. As shown in Fig. 2(b), we also assessed the degree to which the thickness of the WO_3 layer (175 nm, 200 nm, 225 nm and 250 nm) affected the charge capacity ratio when using an NiO/ITO/glass electrode of 60 nm in thickness. With the charge capacity of the NiO

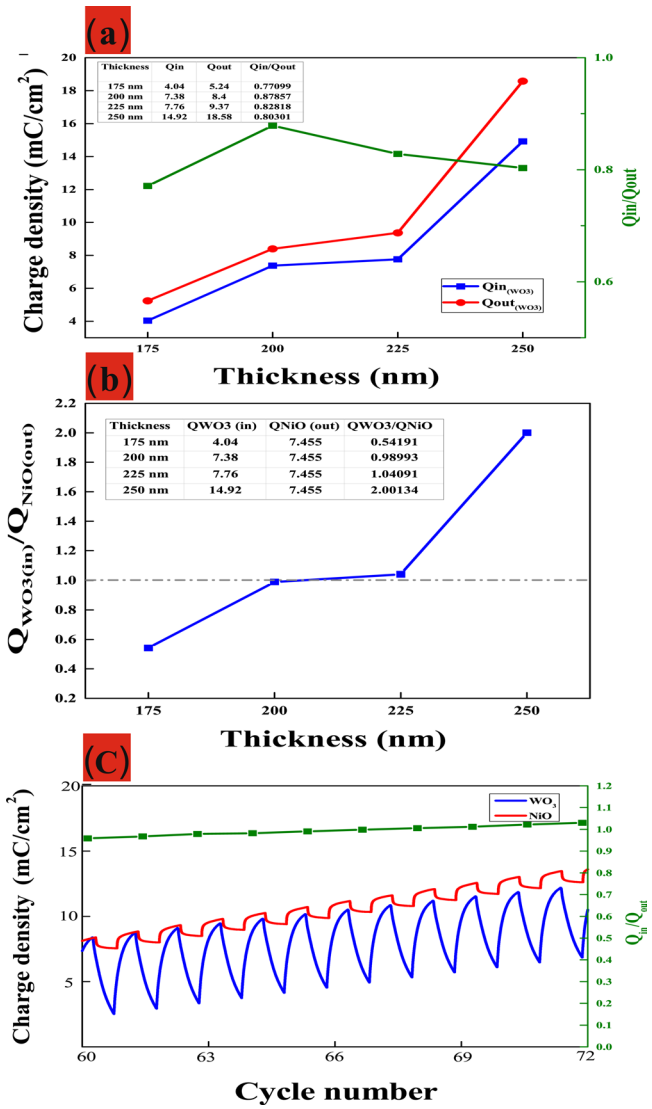

Figure 2. (Color online) (**a**) Surface charge capacity of WO_3/ITO/glass for Q_{in} and Q_{out} (**b**) Complementary charge capacity ration $R = Q_{in}$ (WO_3)/Q_{out}(NiO) (**c**) Reversibility of *R*.

electrode fixed at 7.45 mC cm^{-2}, the *R* values varied as a function of WO_3 thickness, as follows: 175 nm (0.54), 200 nm (0.98), 225 nm (1.04), and 250 nm (2.0). Note that under these conditions, the sample with a 200 nm-thick layer of WO_3 achieved reversibility of nearly 98%. Figure 2(c) shows the reversibility of $R = WO_3$ (200 nm)/NiO (60 nm) about 0.98~1.02 value between 60 and 72 cycles. It appears that the high R value reduced the likelihood of ion blocking, making it an ideal structure for the movement of ions at electrode/electrolyte interfaces in an electrochromic film.

Diffusion coefficient and transmittance optical modulation as a function of WO_3/ITO film thickness. Figure 3(a_1,b_1,c_1,d_1) showed cycle voltammetry (CV) curve of WO_3/ITO films at four different thicknesses and applied the potential voltage from −1.5 V (coloration) to 0.3 V (bleaching) at a scan rate of 200 mV/s. In Fig. 3, the CV curve of WO_3/ITO films were measured at 25^{th}-cycle for four different thicknesses 175 nm, 200 nm, 225 nm, and 250 nm respectively. Furthermore, the diffusion coefficient *D* of Li^+ ions during injection/extraction of ions into/out of the WO_3 film can be calculated using the Randles–Servick Eq. (4)[19].

$$J_p = 2.69 \times 10^5 n^{3/2} C_0 D^{1/2} \nu^{1/2}, \tag{4}$$

where C_0 indicates the concentration of electrolyte solution (mol• cm^{-3}); *v* is the scan rate (V• s^{-1}); *D* is the diffusion coefficient ($cm^2 s^{-1}$) and J_p is the peak current. Table 1 lists the values for J_{pc} (cathodic peak current density), J_{pa} (anodic peak current density), and diffusion coefficient *D* (working area $3 \times 4\,cm^2$). Sample 2 (with 200 nm-thick) of WO_3/ITO films in Table 1 presented the highest ion diffusion coefficients of $7.35 \times 10^{-10}\,cm^2/s$ (oxidation) and $4.92 \times 10^{-10}\,cm^2/s$ (reduction). From Table 1, the higher diffusion coefficient indicates a larger contact area and greater porosity resulting in faster ion insertion/extraction.

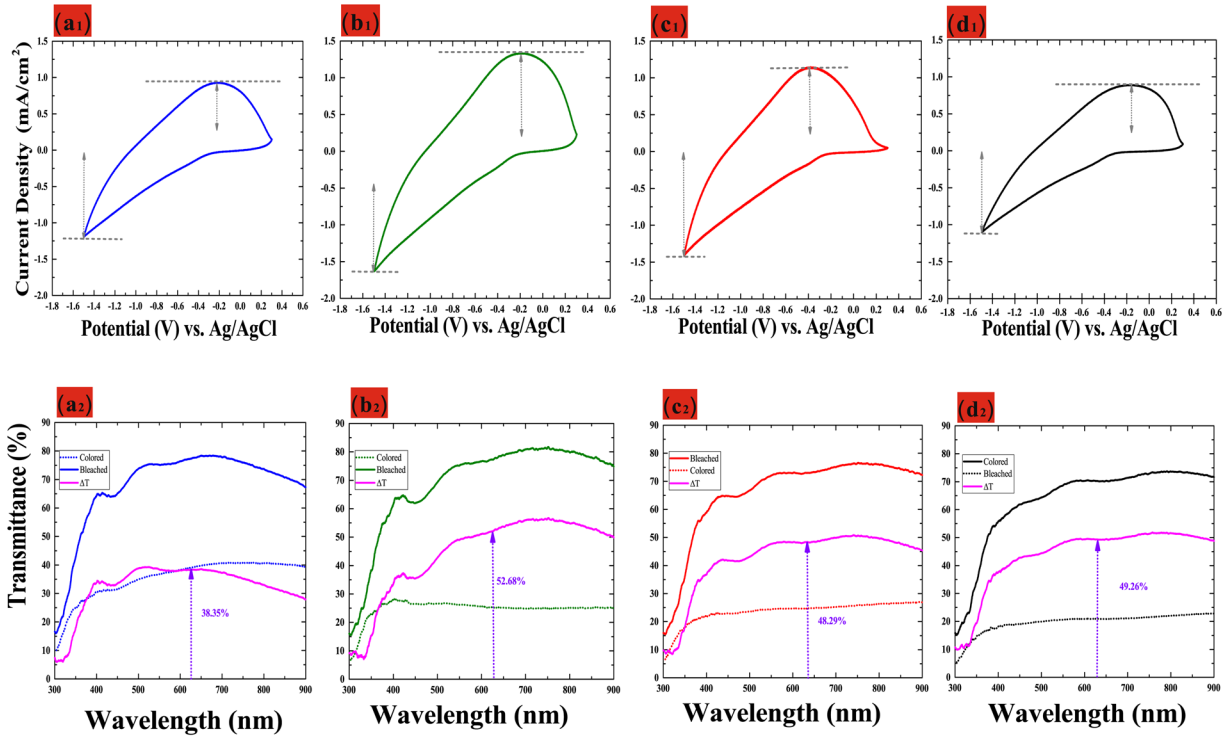

Figure 3. **(a_1,b_1,c_1,$d_{1\ 1,4}$)** CV curves of WO_3 films of various thicknesses during the 25th-cycle; **(a_2,b_2,s_2,d_2)** Transmittance of WO_3 film in bleaching (solid line) and coloration (dotted line) states with various thicknesses.

Sample	Thick(nm)	Cathodic Current(J_{pc})	Anodic Current(J_{pa})	*D* from J_{pc}\J_{pa}	
1	175	1.19×10^{-3}	9.28×10^{-4}	3.92×10^{-10}	2.38×10^{-10}
2	200	1.63×10^{-3}	1.33×10^{-3}	7.35×10^{-10}	4.92×10^{-10}
3	225	1.41×10^{-3}	1.14×10^{-3}	5.46×10^{-10}	3.62×10^{-10}
4	250	1.10×10^{-3}	8.90×10^{-4}	3.36×10^{-10}	2.19×10^{-10}

Table 1. Diffusion coefficients of WO_3/ITO glass of various thicknesses.

Figure 3(a_2,b_2,c_2,d_2) presents the optical transmittance spectra of WO_3/ITO/glass between bleached and colored states at different various thicknesses (175 nm, 200 nm, 225 nm, and 250 nm). At a fixed wavelength of 633 nm, optical transmittance varied as a function of thicknesses from 38.35% to 52.68%. Note that the modulation of optical transmittance of 200-nm-thick WO_3 film ($\Delta T = 52.68\%$) was higher than that of the other samples, as indicated by the larger enveloped area in the CV curve. Actually, the area of the CV curve is deeply related to the charge stored (capacity) at porous WO_3 film[20] indicates that more charges are taking part in redox reactions.

Microstructural characteristics. The cross-sectional SEM image in Fig. 4 shows the hemispherical surface structures of the WO_3 film deposited using CAP. Top-view SEM image of WO_3 pattern inset of Fig. 4. Figure 5(a) presents the X-ray diffraction (XRD) patterns of the WO_3 film deposited on a glass substrate. The porous WO_3 film presented only one broad peak at ~23°, indicating an amorphous structure, as described in previous studies[36]. X-ray photoelectron spectroscopy (XPS) was used to analyze the chemical composition of the WO_3 film surface. The electrochemical testing of Li_xWO_3(WO_3:Li) samples in 0.5 M liquid-electrolyte of $LiClO_4$/PC solution was performed using a three-electrode cell, comprising a working electrode (WO_3 electrode film on ITO/glass), a counter-electrode (Pt mesh) and a reference electrode (Ag/AgCl). The color of the WO_3/ITO/glass changed from deep blue (colored state; $-1.35\ V$) to transparent (bleached state; $0.2\ V$), is accordance with the intercalation/extraction of ions (Li^+) into/out of the WO_3 electrode. The thickness of the WO_3 film was shown to have considerable influence on the electrochromic properties by XPS analysis. Figure 5(c,e) show XPS spectra of W 4 f in tungsten oxide films (200 nm) and (250 nm) in coloration states. In Fig. 5(c,e), the peaks W $4f_{7/2}$ and W $4f_{5/2}$ of W^{6+} and W^{5+} that are located at binding energies of 35.17 and 37.24 eV corresponding to W4 $f_{5/2}$ and W4 $f_{7/2}$ of W^{5+} in the Li_xWO_3. The coloration process indicates the movement of Li^+ ions and electrons into the WO_3 films, such that the W^{6+} obtained an e^- to become W^{5+}, resulting in a corresponding shift in the peak to a lower energy level. The content of W^{5+} in Li_xWO_3 film (i.e., $\eta(W^{5+})$) can be calculated using the following equation:

$$\eta(W^{5+}) = W^{5+}/(W^{5+} + W^{6+}) \times 100\%. \quad (5)$$

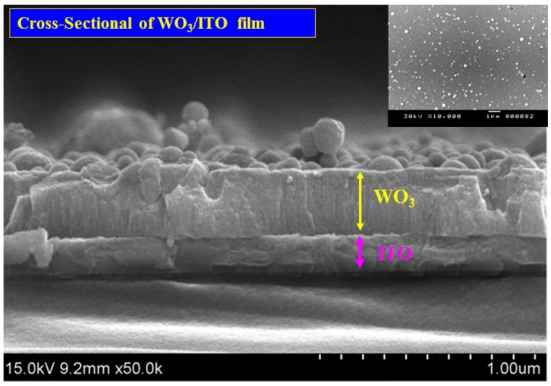

Figure 4. Cross-sectional morphologies of WO_3/ITO film.

The fitted spectrum can be separated into two gaussian doublets shown Fig. 5(c–f). In this redox reaction Eq.(5), we evaluated ions transformed from the W^{6+} to the W^{5+} state. In Fig. 5(c–e), we calculated that approximately 30% (200 nm) and 35% (250 nm) of the ions transformed from the W^{6+} to the W^{5+} state, see Table 2. This is an indication that a larger number of W^{6+} (bleaching) Li^+ ions took part in the reduction reaction to become W^{5+} (blue). As shown in Fig. 3(b_2,d_2), we found that as the thickness of the film increased, Q_{in} (WO_3) curve gradually increased as did the power of lithium-ion injection, optical transmittance of 200-nm-thick WO_3 film ($T_{coloration} = 25.12\%$) and 250-nm-thick WO_3 film ($T_{coloration} = 18.13\%$) at a fixed wavelength of 633 nm. Figure 5(d–f) presents high-resolution XPS spectra of W 4 f in tungsten oxide films (200 nm) and (250 nm) in bleaching states. In the W 4 f spectrum in the beached state (Fig. 5(d)), the peaks at binding energies of 35.6 and 37.7 eV correspond to W4 $f_{5/2}$ and W4 $f_{7/2}$ of W^{6+}. Thus, we can deduce that only W^{6+} ions were present in the WO_3 thin films in the bleached state. But when the film thickness reaches 250 nm, the film can't completely fade, which is still light blue, which means that W^{5+} (blue) can't completely convert to W^{6+} (bleaching).

This is confirmed by the detection of W^{5+} in a later XPS analysis of the 250 nm bleached film. This shows that there are residual W^{5+}ions in the process of fading oxidation when lithium ion is injected into the coloring reduction reaction Therefore, appropriate film thickness, will help improve the electrochromic optical modulation performance. The 200-nm-thick film contained only W^{6+} ions; however, some of the W^{5+} ions in the 250-nm-thick film did not convert into W^{6+} ions, thereby decreasing the penetration of the bleaching state, as shown in Fig. 3(b_2,d_2), we found optical transmittance of 200-nm-thick WO_3 film ($T_{bleaching} = 78.85\%$) and 250-nm-thick WO_3 film ($T_{bleaching} = 70.05\%$) at a fixed wavelength of 633 nm. In Fig. 5(f), we calculated that approximately 80% (250 nm) of the ions transformed from the W^{5+} to the W^{6+} state, see Table 2. Ning *et al.*[42] claimed that lattice strain can affect the diffusion and migration of lithium ions, such that the coefficient of lithium ion diffusion decreases under the effects of pressure-induced strain. Thus, the failure of the 250-nm-thick film to recolor may be due to the thickness of the film, which extended the lithium ion migration path, such that the remaining stress hindered the transfer of lithium ions and the conversion of W^{5+} to W^{6+}. Therefore, tungsten oxide film as a cathodic electrochromic layer, the film thickness should be selected appropriately, can improve modulation optical transmittance to optimization conditions.

Coloration efficiency of WO_3/ITO films as a function of thickness. Coloration efficiency (CE) is an important criterion in the evaluation of electrochromic materials. CE is defined as the optical density charge (ΔOD) per unit of inserted charge Q_{in} ($Q_{in} = Q/A$, where A is the [20]:

$$CE = \Delta OD/Q_{in}$$
$$\Delta OD = \ln(T_{\text{bleaching}}/T_{\text{coloration}}). \quad (6)$$

where $T_{\text{bleaching}}$ and $T_{\text{coloration}}$ refer to the transmittance of bleaching and coloration state. Generally, a high CE value is an indication of large optical modulation under small charge insertion. Figure 6(a–d) plots ΔOD at a wavelength of 633 nm as a function of the charge inserted into films. The CE value of the as-synthesized WO_3/ITO/glass was estimated from the slopes of the quasi-linear curves. The CE values at 633 nm were as follows: 175 nm (79.8 $cm^2\ C^{-1}$), 200 nm (90 $cm^2\ C^{-1}$), 225 nm (77.5 $cm^2\ C^{-1}$), and 250 nm (72.3 $cm^2\ C^{-1}$).

Characterization of WO_3/NiO ECD. Figures 7,8 presents the electrochromic performance of ECD (glass/ITO/WO_3/liquid electrolyte/NiO/ITO/glass) with an active area of $3 \times 4\ cm^2$. Figure 7(a) presents the *in-situ* transmittance of WO_3/NiO ECD at 633 nm, as analyzed during a continuous potential cycle from $-1.5\ V$ (colored potential, V_c) to 0.8 V (bleached potential, V_b). In Fig. 7(b,c) show that the coloration state (charge process) and bleaching state (discharge process) of ECDs were measured by CA curves and *in-situ* optical response of transmittance at fixed 633 nm. The coloration and bleaching of switching times or speed was a prominent characteristic for ECD system, which was defined as the time required for a 90% change in the full transmittance modulation[43–45]. As shown in Fig. 7(c), ECD achieved a maximum optical modulation reached 46% and the switching times at a wavelength of 633 nm were obtained coloration (3.1 sec) and bleaching (4.6 sec) (see supplementary video). The electrochromic and optical properties of our work compared with other authors researches are detailed in

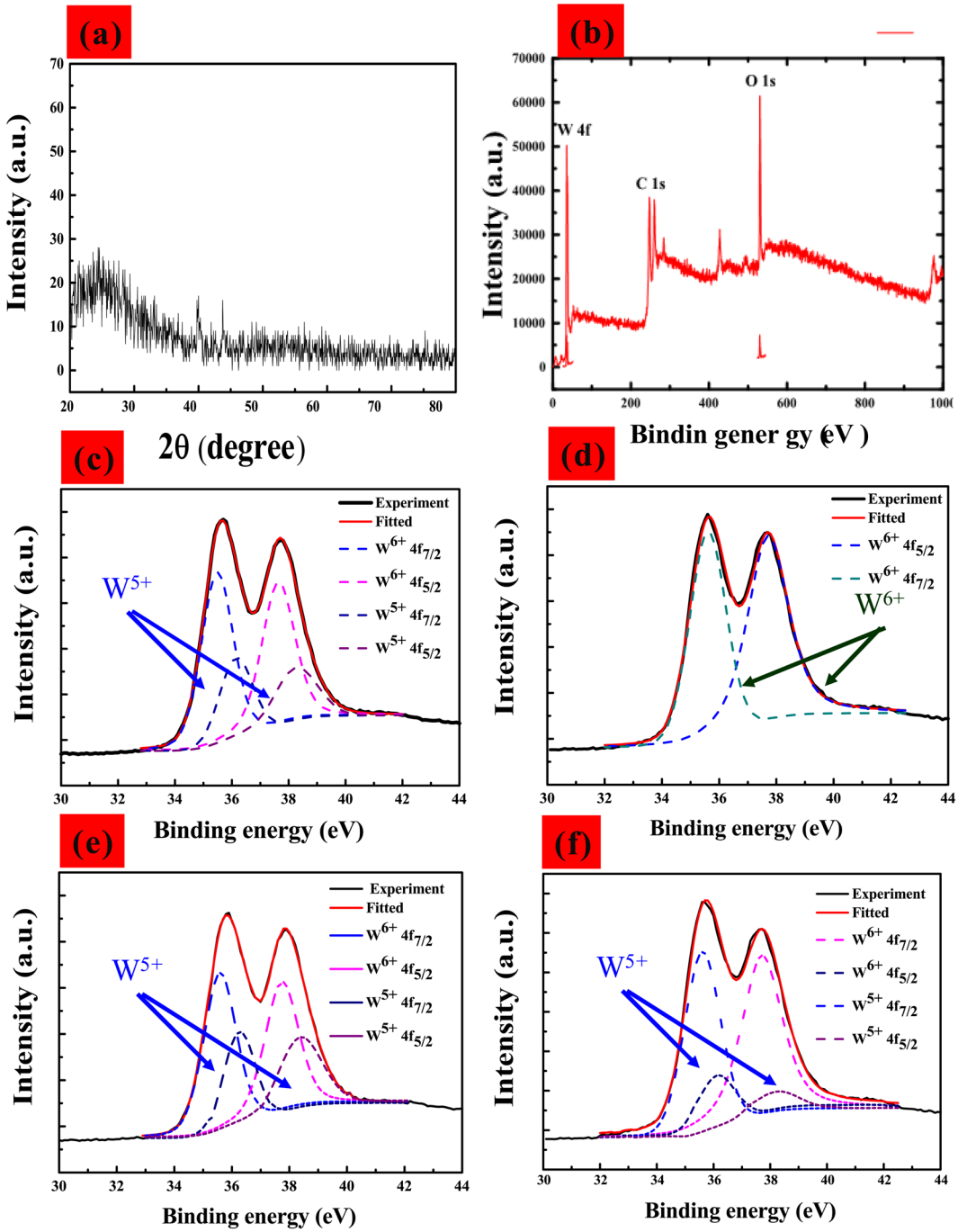

Figure 5. (Color online) (**a**) XRD pattern of WO_3/glass film (**b**) Wide scanning XPS spectra of WO_3 film (**c**,**e**) High-resolution XPS W4f spectra of coloration WO_3 film at 200-nm-thick and 250-nm-thick. (**d**,**f**) High-resolution XPS W4f spectra of bleaching WO_3 film at 200-nm-thick and 250-nm-thick.

Table 3. Figure 8 illustrates the durability of the ECDs in terms of transmittance optical modulation measured in intervals of 15 s. As shown in Fig. 8, even after 1000 cycles (approximately 10 hours), there was no significant degradation in the optical modulation performance of the ECD. As shown in Fig. 8, transitions between bleached and colored states remained steady until 1000 cycles, at which point switching performance degraded gradually, dropping to 93% of the as-synthesized samples by 2500 cycles.

Methods

Cathodic arcs can be used for the reactive deposition of various nitrides and oxides. Nonetheless, CAP technology has not been widely adopted, due to violent plasma-liquid pool interactions at cathode spots, which can cause the emission of macro-particles (MPs) that degrade the quality of the resulting film. This can largely be overcome by steering the arc rapidly across the surface of the cathode under high working pressure to reduce the spot residence

Thick (nm)	states	W oxidation	W 4 f	Bindingenergy (eV)	FWHM (eV)	Aera (%)
200	Bleaching	W^{6+}	$\frac{W4f_{7/2}}{W4f_{5/2}}$	$\frac{35.6}{37.7}$	$\frac{0.8}{0.8}$	100%
200	Coloration	W^{6+}	$\frac{W4f_{7/2}}{W4f_{5/2}}$	$\frac{35.5}{37.7}$	$\frac{1.6}{1.8}$	70%
200	Coloration	W^{5+}	$\frac{W4f_{7/2}}{W4f_{5/2}}$	$\frac{36.2}{38.4}$	$\frac{2.2}{2.2}$	30%
250	Bleaching	W^{6+}	$\frac{W4f_{7/2}}{W4f_{5/2}}$	$\frac{35.6}{37.7}$	$\frac{1.7}{2}$	80%
250	Bleaching	W^{5+}	$\frac{W4f_{7/2}}{W4f_{5/2}}$	$\frac{36.2}{38.2}$	$\frac{1.8}{2}$	20%
250	Coloration	W^{6+}	$\frac{W4f_{7/2}}{W4f_{5/2}}$	$\frac{35.6}{37.8}$	$\frac{1.7}{2}$	65%
250	Coloration	W^{5+}	$\frac{W4f_{7/2}}{W4f_{5/2}}$	$\frac{36.3}{38.4}$	$\frac{1.8}{1.9}$	35%

Table 2. W 4*f* peak fitting binding energy of WO_3 film with thick of 200 and 250 nm. *FWHM-Full width half maximum.

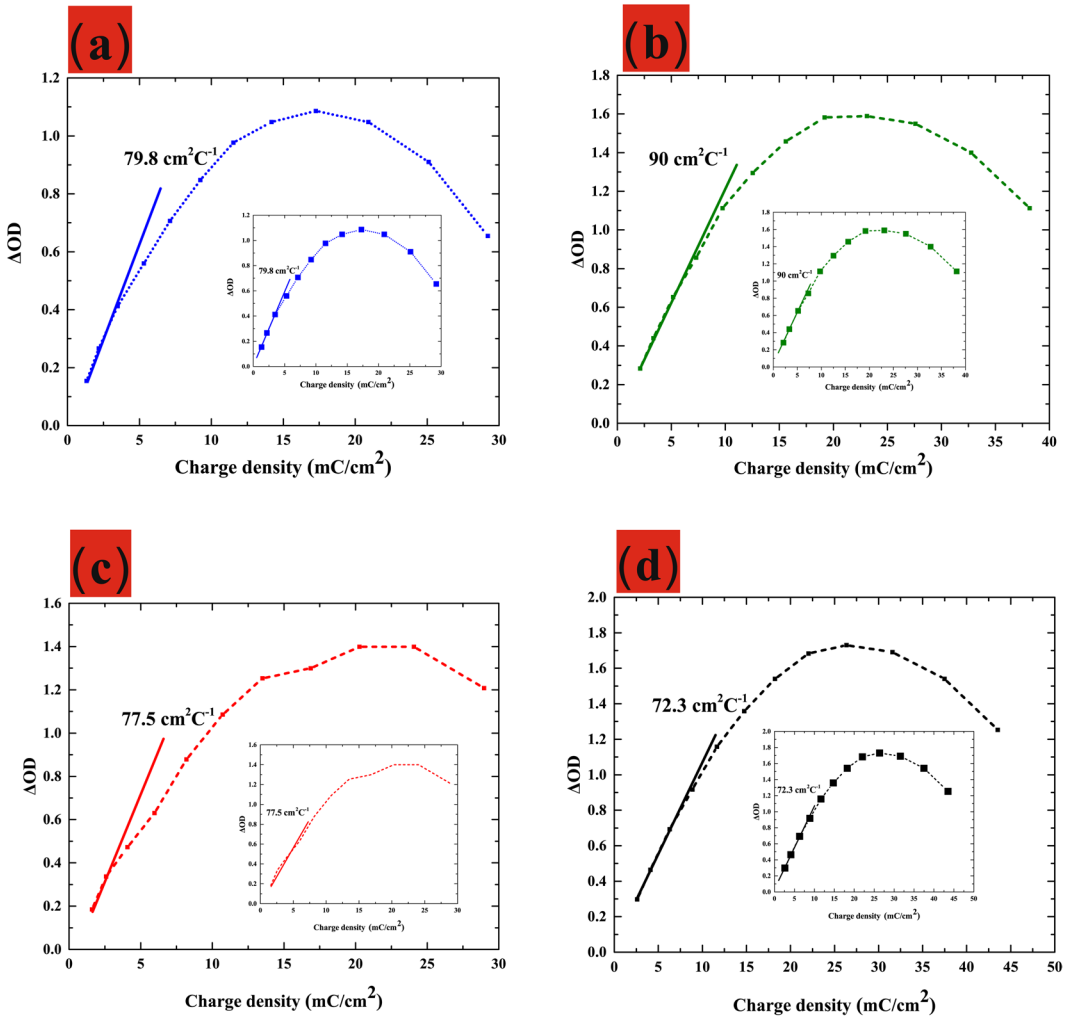

Figure 6. (Color online) Optical density change as a function of inserted charge for WO_3/ITO film with various thicknesses.

time and limit the formation of erosion craters[46]. In recent years, researchers have shifted emphasis from monolithic coatings to higher performing multilayers and nano-composites. As shown in Fig. 9(a), the proposed arc gun set up relies on the flow of argon (for insertion) and oxygen (reaction) to control the formation of the electrode structure. It is difficult to measure the dynamics of a cathode spot; therefore, we employed a high-speed

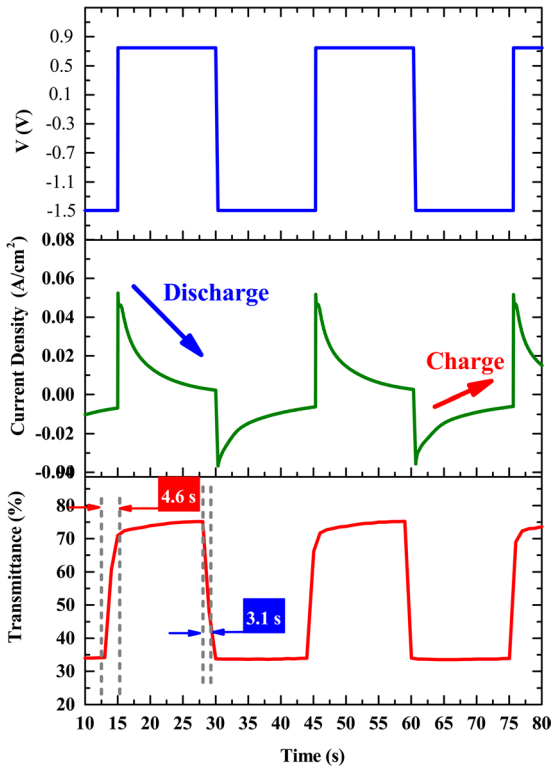

Figure 7. (Color online) (**a**) While the optical modulation for applied voltage of −1.5 V for colored state and 0.8 V for bleached state within interval of each step was controlled at 15 s; (**b**) corresponding CA curve of ECD; (**c**) switching time between bleached and colored states measured at 633 nm between 0.8 V and −1.5 V.

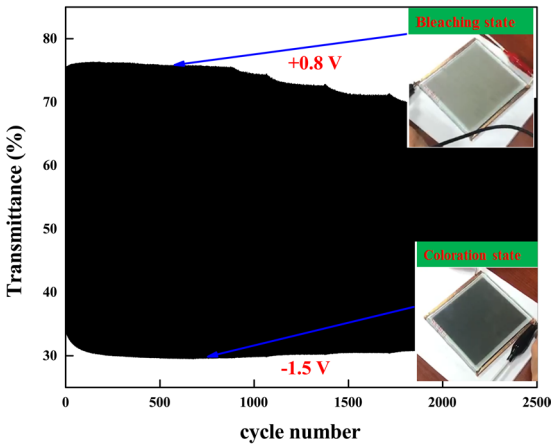

Figure 8. The durability of ECDs in terms of transmittance optical modulation at 633 nm following 2500-cycles.

video camera to capture images of light emission from various spots across the target plane in sequences of 1 sec, as shown in Fig. 9(b,c). The deposition parameters are shown in Table 2 and 3, and the schematic drawing of the cathodic arc deposition is presented in Fig. 9(a).

Figure 10 presents a schematic diagram showing the process of ECD fabrication. Figure 10(a): Step 1 and 2 involved respectively depositing an EC film/ITO on one glass substrate and a counter film/ITO on another glass substrate. Step 3 involved fitting the two components together and sealing them with epoxy adhesive. Note glass beads were used as spacers to maintain a cavity between the EC film and the counter film to hold liquid electrolyte ($<100\,\mu$m). Note also that a small gap was created in the epoxy for use as an inlet into the space. Step 5 showed ECD consisted of seven layers: A central ionic conduction layer (electrolyte) sealed between an electrochromic (EC) layer and an ion storage (complementary) layer, which were sandwiched between two transparent conducting layers, which were in turn sandwiched between two glass substrates. Figure 10(b) mainly describes the process of component packaging. Figure 10(b) Step 1: Dispensing for one side pre gluing. Step 2: UV glue curing. Step 3

Materials/Device	Method	$\frac{\Delta T}{(\%)}$	$\frac{CE}{\left(cm^2/C\right)}$	$\frac{Switchingtime}{(t_c/t_b)}$	Ref.
WO_3/NiO	CAP	46	90	3.1/4.6 s	This work
Mo-doped WO_3	RF sputtering	44.3	42.5	—	[24]
WO_3/NiO	DC sputtering	55	87	10/20 s	[25]
WO_3/PANI	Electropolymerization	37.4	98.4	9.9/13.6 s	[42]
WO_3/MoO_3	physicochemical	50	121.56	4.1 /3.4 s	[47]
WO_3	Electrodeposition	88.51	137	3.7/5.2 s	[48]
WO_x nanorods	Exposure	57	33.3	11.8 /20.1 s	[49]
WO_3 $0.33H_2O$/PEDOT	sol-gel	50.9	74.6	5/25 s	[50]
Tb-doped WO_3	hydrothermal	66.71	48.33	3.7/9.99 s	[51]
WO_3/PANI	dip-coating	54.3	79.7	1.4/1.1 s	[43]
WO_3	spray	64	—	—	[44]
$(NH_4)_{0.33}WO_3$	hydrothermal	51.6	60.9	5.7/4.2 s	[45]

Table 3. exhibits the comparison of our results with the literature on various materials and methods[43–45,47–51].

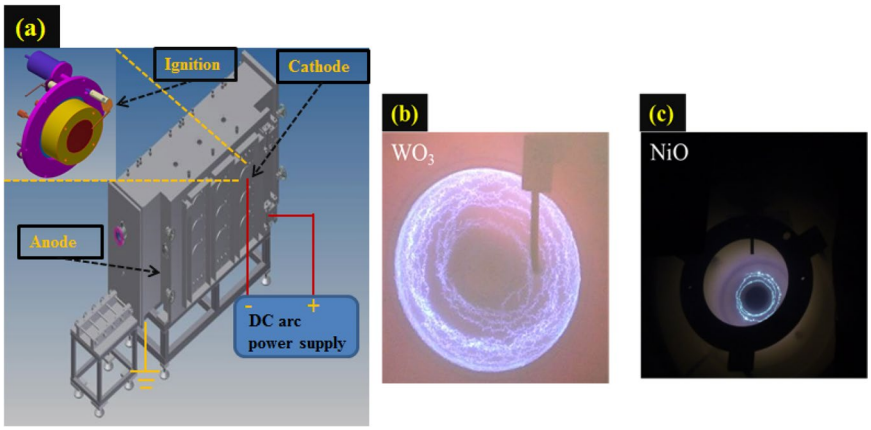

Figure 9. (**a**) Cathodic arc plasma (CAP) gun; (**b,c**) WO_3/ NiO images showing the transient dynamics of cathodic spot motion.

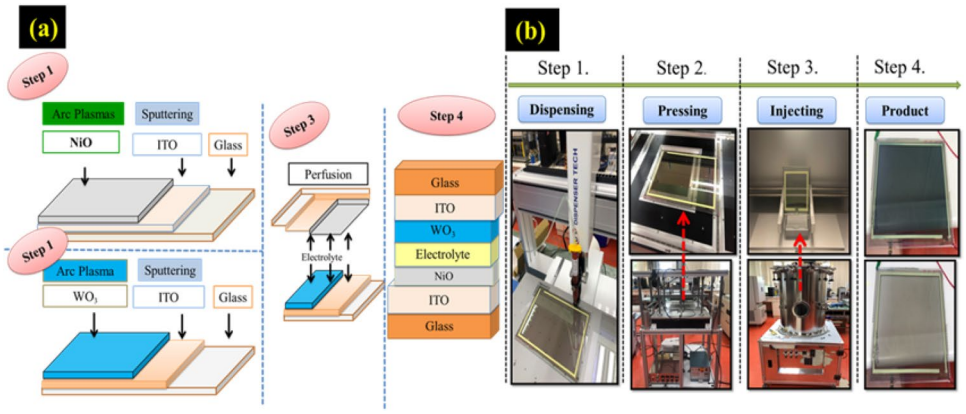

Figure 10. (**a**) Experimental procedure for Step1 to Step4. (**b**) Packaging process for ECD.

involved filling the space between the two layers with liquid electrolyte ion injection in a vacuum pump. Step 4 production components.

Synthesis of porous electrochromic and dense transparent electrodes films. Indium tin oxide (ITO, Solaronix SA, $R_{sh} = 6.1\ \Omega/\square$)-coated glass was cut into wafers ($5 \times cm^2$) for use as a conducting substrate in ECDs. The ITO wafers underwent ultrasonic cleaning respectively in deionized water and ethyl alcohol for 2 min each. WO_3/NiO films were deposited in series on the ITO glass using cathodic arc plasma (CAP) with targets of metallic tungsten (W) (99.95%) and Nickel (Ni) (99.95%) (76 mm in diameter and 12 mm in thickness) at room

WO_3 Pro.	W.P. (Torr)	$\frac{Ar}{O_2}$	DC power (W)	Time (min)	Dep. Rate (nm/min)	Dep. Temp. °C
Sample 1	8.3×10^{-3}	0.2	1250	11	15.9	25
Sample 2	8.3×10^{-3}	0.2	1250	13	15.4	25
Sample 3	8.3×10^{-3}	0.2	1250	15	15	25
Sample 4	8.3×10^{-3}	0.2	1250	17	14.7	25

Table 4. Details of WO_3 processing parameters.

Target	W.P. (Torr)	Ar/O_2 (sccm)	DC power (W)	Time (min)	Deposition. Rate (nm/min)	Dep. Temp. °C	Thick (nm)
ITO	3×10^{-3}	$Ar = 100$	500	60	5	200	300
Ni Metal	8.3×10^{-3}	$1/3(Ar = 120)$	650	2.5	20	50	60

Table 5. More details of ECD deposition parameters.

temperature, as shown Fig. 10(a). The base chamber pressure was maintained at less than 2×10^{-5} Torr using a turbo pump. Tables 4 and 5 list the fabrication parameters. CAP was used to deposit WO_3/NiO as working/counter electrodes. As shown in the schematic in Fig. 10(a), the active area of the ECD ($3 \times 4\,cm^2$) possessed the following structure: glass/ITO/WO_3/liquid electrolyte/NiO/ITO/glass. Our primary focus in the current study was the analysis of WO_3 films in terms of charge capacity and diffusion coefficient. The WO_3/NiO series were fabricated on ITO glasses as electrochromic layers, which are listed in Tables 4 and 5.

Electrolyte layer. The liquid electrolyte system comprised lithium perchlorate ($LiClO_4$, Mw = 106.39, Sigma-Aldrich, Darmstadt, Germany) and propylene carbonate (PC, $C_4H_6O_3$, Sigma-Aldrich) at a weight ratio of 0.1325 ($LiClO_4$/PC = 26.5 g/200 mL).

Measurements. Electrochemical characterization was performed using cycle voltammetric (CV) and chronoamperometric (CA) (Autolab, model PGSTAT 30) measurements. *In–situ* UV-Vis measurements were obtained using a spectrophotometer (Ocean Optics, DH-4000-BAL) in conjunction with CA analysis.

Conclusions

In conclusion, we have developed a CAP deposition as an alternative to sputtering in order to achieve high deposition rates with low-cost method of producing EC film based on WO_3 for ECD applications. The proposed deposition scheme was applied to the synthesis of WO_3 films with nanostructured surface features in various thicknesses (175 nm, 200 nm, 225 nm, and 250 nm). The complementary WO_3(200 nm)/NiO (60 nm) ECD exhibits higher optical modulation (46% at 633 nm), faster response times ($t_b = 4.6\,s$, $t_c = 3.1\,s$) and higher CE (90 cm^2/C). During the durability test, the transmittance change of ECD remained 43% after 2500 cycles, which was about 93% of original state.

Received: 13 January 2020; Accepted: 28 April 2020;
Published online: 21 May 2020

References

1. Lampert, C. M. Large-area smart glass and integrated photovoltaics. *Solar Energy Materials and Solar Cells.* **76**, 489–499 (2003).
2. Runnerstrom, E. L. *et al.* Nanostructured electrochromic smart windows: traditional materials and NIR-selective plasmonic nanocrystals. *Chem. Commun.* **50**, 10555–10572 (2014).
3. Haizeng, L. *et al.* Nanohybridization of molybdenum oxide with tungsten molybdenum oxide nanowires for solution-processed fully reversible switching of energy storing smart windows. *Nano Energy* **47**, 130–139 (2020).
4. Lee, E. S. & DiBartolomeo, D. L. Application issues for large-area electrochromic windows in commercial buildings. *Sol. Energy Mater. Sol. Cells* **71**, 465–491 (2002).
5. Jelle, B. P. & Hagen, G. Transmission spectra of an electrochromic window based on polyaniline, Prussian blue and tungsten-oxide. *J. Electrochem. Soc.* **140**, 3560–3564 (1993).
6. Rosseinsky, D. R. & Mortimer, R. J. Electrochromic systems and the prospects for devices. *Adv. Mater.* **13**, 783–793 (2001).
7. Granqvist, C. G. Electrochromic tungsten oxide films: review of progress 1993 -1998. *Solar Energy Materials and Solar Cells* **60**, 201–262 (2000).
8. Vidotti, M. Cordoba de Torresi, S. I. Electrostatic layer-by-layer and electrophoretic depositions as methods for electrochromic nanoparticle immobilization. *Electrochim. Acta* **54**, 2800–2804 (2009).
9. Bouessay, I. *et al.* Electrochromic degradation in nickel oxide thin film: a self-discharge and dissolution phenomenon. *Electrochim. Acta* **50**, 3737–3745 (2005).
10. Watanabe, Y., Imaizumi, K., Nakamura, K. & Kobayashi, N. Effect of counter electrode reaction on coloration properties of phthalate-based electrochromic cell. *Solar Energy Materials and Solar Cells* **99**, 88–94 (2012).
11. Kobayashi, T., Yoneyama, H. & Tamura, H. Polyaniline film-coated electrodes as electrochromic display devices. *J. Electroanal. Chem.* **161**, 419–423 (1984).
12. Silva, A. J. C. *et al.* A multielectrochromic copolymer based on pyrrole and thiophene derivatives. *Solar Energy Materials and Solar Cells* **103**, 108–113 (2012).
13. Augusto, T. *et al.* Electrophoretic deposition of Au@PEDOT nanoparticles towards the construction of high-performance electrochromic electrodes. *Solar Energy Materials and Solar Cells* **118**, 72–80 (2013).
14. Granqvist C. G. Handbook of Inorganic Electrochromic Materials, Elsevier, Amsterdam, the Netherlands (1995).

15. Xia, X. H. *et al*. Electrochromic properties of porous NiO thin films prepared by a chemical bath deposition. *Solar Energy Materials and Solar Cells* **92**, 628–633 (2008).
16. Subrahmanyam *et al*. A note on fast protonic solid state electrochromic device: $NiO_x/Ta_2O_5/WO_{3-x}$. *Solar Energy Materials and Solar Cells* **91**, 62–66 (2007).
17. Li, H., McRae, L. & Elezzabi, A. Y. Solution-processed interfacial PEDOT: PSS assembly into porous tungsten molybdenum oxide nanocomposite films for electrochromic applications. *ACS applied materials & interfaces* **10**, 10520–10527 (2018).
18. Eren, E. *et al*. High-performance Flexible Complementary Electrochromic Device Based on Plasma Modified WO_3 Nano Hybrids and V_2O_5 Nanofilm with Low Operation Voltages. *Electroanalysis* **30**, 2099–2109 (2018).
19. Liu, B. *et al*. Controlled fabrication of hierarchical WO_3 hydrates with excellent adsorption performance. *J. Mater. Chem. A* **2**, 1947–1954 (2014).
20. Deniz, D. *et al*. Nanostructured tungsten and tungsten trioxide films prepared by glancing angle deposition. *Thin Solid Films* **518**, 4095–4099 (2010).
21. Wei, H. *et al*. Electropolymerized polyaniline stabilized tungsten oxide nanocomposite films: electrochromic behavior and electrochemical energy storage. *J. Phys. Chem. C* **116**, 25052–25064 (2012).
22. Lin, F. *et al*. Low-temperature ozone exposure technique to modulate the stoichiometry of WO_x nanorods and optimize the electrochromic performance. *Nanotechnology* **23**, 255601 (2012).
23. Yaacob, M. H. *et al*. Absorption spectral response of nanotextured WO_3 thin films with P_t catalyst towards H_2. *Sensors and Actuators B: Chemical* **137**, 115–120 (2009).
24. Madhavi, V., Kumar, P. J., Kondaiah, P., Hussain, O. M. & Uthanna, S. Efect of molybdenum doping on the electrochromic properties of tungsten oxide thin flms by RF magnetron sputtering. *Ionics* **20**, 1737–1745 (2014).
25. Zhang, J., Tu, J., Xia, X., Qiao, Y. & Lu, Y. An all-solid-state electrochromic device based on NiO/WO_3 complementary structure and solid hybrid polyelectrolyte. *Solar Energy Materials and Solar Cells* **93**, 1840–1845 (2009).
26. Lin, Y. S. *et al*. Electrochromic properties of novel atmospheric pressure plasma jet-synthesized-organotungsten oxide films for flexible electrochromic device. *Solar Energy Materials and Solar Cells* **94**, 2283–2291 (2010).
27. White, C. M., Gillaspie, D. T., Whitney, E., Lee, S. H. & Dillon, A. C. *Thin Solid Films* **517**, 3596 (2009).
28. Bathe, S. R. *et al*. Electrochromic characteristics of fibrous reticulated WO_3 thin films prepared by pulsed spray pyrolysis technique. *Solar Energy Materials and Solar Cells* **91**, 1097 (2007).
29. Kadam, P. M. *et al*. From beads-to-wires-to-fibers of tungsten oxide: electrochromic response. *Applied Physics A* **97**, 323–330 (2009).
30. Thangala, J. *et al*. Large-scale, hot-filament-assisted synthesis of tungsten oxide and related transition metal oxide nanowires. *Small* **3**, 890–896 (2007).
31. Patel, K. J. *et al*. An investigation of the insertion of the cations H^+, Na^+, K^+ on the electrochromic properties of the thermally evaporated WO_3 thin films grown at different substrate temperatures. *Mater. Chem. Phys.* **124**, 884–890 (2010).
32. Zheng, H. D. *et al*. Nanostructured Tungsten Oxide – Properties, Synthesis, and Applications. *Adv. Funct. Mater.* **21**, 2175–2196 (2011).
33. Li, J. T. *et al*. Evolution of the nanostructure of deposits grown by electron beam induced deposition. *Appl. Phys.Lett.* **93**, 023130–023130-3 (2008).
34. Fan, H. *et al*. Three-Dimensionally Ordered Gold Nanocrystal/Silica Superlattice Thin Films Synthesized via Sol–Gel Self-Assembly. *Adv. Funct. Mater.* **16**, 891–895 (2006).
35. Xie, Z. *et al*. Porous WO_3 with enhanced photocatalytic and selective gas sensing properties. *CrystEngComm* **13**, 6393–6398 (2011).
36. Cai, G. F. *et al*. Efficient electrochromic materials based on $TiO_2@WO_3$ core/shell nanorod arrays. *Solar Energy Materials and Solar Cells* **117**, 231–238 (2013).
37. Paipitak, K. *et al*. Characterization of sol-gel derived ti-doped tungsten oxide electrochromic thin flms. *Energy. procedia.* **9**, 446–451 (2011).
38. Lee, K. D. *et al*. Indium-Zinc-Tin-Oxide film prepared by DC reactive magnetron sputtering for electrochromic application. *materials* **11**, 2221–22211 (2018).
39. Chen, P. W. *et al*. Tantalum oxide film deposited by vacuum cathodic arc plasma with improved electrochromic performance. *Solar Energy Materials and Solar Cells* **182**, 188–195 (2018).
40. Chen, P. W. *et al*. Inorganic-solid-state electrolyte layer deposited by cathodic arc plasma for rapidly switching electrochromic device. *AIP Proceedings* **1879**, 0300041–0300045 (2017).
41. Wang, C. *et al*. Stepwise and Statistical Simulation on the Random and Retrograde Motion of a Single Cathode Spot of Vacuum Arc. *IEEE Transactions on Plasma Science* **43**, 2267–2274 (2015).
42. Yang, L. *et al*. Improved electrochromic performance of ordered macroporous tungstenoxide films for IR electrochromic device. *Solar Energy Materials and Solar Cells* **100**, 251–257 (2012).
43. Wang, W. Q. *et al*. Enhanced electrochromic and energy storage performance in mesoporous WO_3 film and its application in a bi-functional smart window. *Nanoscale* **10**, 8162–8169 (2018).
44. Hyungsub, K. *et al*. Effect of particle size and amorphous phase on the electrochromic properties of kinetically deposited WO_3 films. *Solar Energy Materials and Solar Cells* **177**, 44–50 (2018).
45. Dongyun, M. *et al*. Electrochromic devices based on tungsten oxide films with honeycomb-like nanostructures and nanoribbons array. *Solar Energy Materials and Solar Cells* **177**, 51–56 (2018).
46. Anders, A. *et al*. Cathode mode transition in high-pressure discharge lamps at start up. *Light. Res. Technol.* **22**, 111–115 (1990).
47. Kharade, R. R. *et al*. Hybrid physicochemical synthesis and electrochromic performance of WO_3/MoO_3 thin flms. *Electroanal* **26**, 2388–2397 (2014).
48. Dalavi, D. S. *et al*. Efcient electrochromic performance of nanoparticulate WO_3 thin flms. *J. Mater. Chem. C* **1**, 3722–3728 (2013).
49. Chang, X., Sun, S., Dong, L., Hu, X. & Yin, Y. Tungsten oxide nanowires grown on graphene oxide sheets as high-performance electrochromic material. *Electrochim. Acta* **129**, 40–46 (2014).
50. Yanfang, Y. *et al*. High-performance complementary electrochromic device based on WO_3 $0.33H_2O$/PEDOT and prussian blue electrodes. *Journal of Physics and Chemistry of Solids* **110**, 284–289 (2017).
51. Luying, S., Jianming, Z. & Chunye, X. Enhanced electrochromic switches and tunable green fluorescence based on terbium ion doped WO_3 films. *Nanoscale* **11**, 23049–23057 (2019).

Acknowledgements

PWC would also like to acknowledge support from Division of Physics, Institute of Nclear Energy Research, Taiwan. This study was partially supported by the Ministry of Science and Technology (MOST) of Taiwan under grant MOST 106-2221-E-006-053-MY3.

Author contributions

The study was writting and review by P.-W.C.; the data collection and analysis for WO_3 film by C.-T.C.; T.-F. K. prepared Figures 3 and 10; the experiments was performed by S.-C.H. and J.-Y.W.;K.-D. Li performed the XPS characterization.

Competing interests

The authors declare no competing interests.

Additional information

Supplementary information is available for this paper at https://doi.org/10.1038/s41598-020-65191-x.

Correspondence and requests for materials should be addressed to P.-W.C.

Reprints and permissions information is available at www.nature.com/reprints.

Publisher's note Springer Nature remains neutral with regard to jurisdictional claims in published maps and institutional affiliations.